Geophysical Journal International

Investigating long-term subsidence at Medicine Lake Volcano, CA, using multitemporal InSAR

Amy L. Parker,[1] Juliet Biggs[1] and Zhong Lu[2]

[1]*COMET, School of Earth Sciences, University of Bristol, Wills Memorial Building, Bristol, BS8 1RJ, United Kingdom. E-mail: Amy.Parker@bristol.ac.uk*
[2]*Roy M. Huffington Department of Earth Sciences, Southern Methodist University, PO Box 750395, Dallas, TX 75275-0395, USA*

SUMMARY

Long-term volcanic subsidence provides insight into intereruptive processes, which comprise the longest portion of the eruptive cycle. Ground-based geodetic surveys of Medicine Lake Volcano (MLV), northern CA, document subsidence at rates of ~-10 mm yr^{-1} between 1954 and 2004. The long observation period plus the duration and stable magnitude of this signal presents an ideal opportunity to study long-term volcanic deformation, but this first requires accurate knowledge of the geometry and magnitude of the source. Best-fitting analytical source models to past levelling and GPS data sets show conflicting source parameters—primarily the model depth. To overcome this, we combine multiple tracks of InSAR data, each with a different look angle, to improve upon the spatial resolution of ground-based measurements. We compare the results from InSAR to those of past geodetic studies, extending the geodetic record to 2011 and demonstrating that subsidence at MLV continues at ~-10 mm yr^{-1}. Using geophysical inversions, we obtain the best-fitting analytical source model—a sill located at 9–10 km depth beneath the caldera. This model geometry is similar to those of past studies, providing a good fit to the high spatial density of InSAR measurements, while accounting for the high ratio of vertical to horizontal deformation derived from InSAR and recorded by existing levelling and GPS data sets. We discuss possible causes of subsidence and show that this model supports the hypothesis that deformation at MLV is driven by tectonic extension, gravitational loading, plus a component of volume loss at depth, most likely due to cooling and crystallization within the intrusive complex that underlies the edifice. Past InSAR surveys at MLV, and throughout the Cascades, are of variable success due to dense vegetation, snow cover and atmospheric artefacts. In this study, we demonstrate how InSAR may be successfully used in this setting by applying a suite of multitemporal analysis methods that account for atmospheric and orbital noise sources. These methods include: a stacking strategy based upon the noise characteristics of each data set; pixelwise rate-map formation (π-RATE) and persistent scatterer InSAR (StaMPS).

Key words: Satellite geodesy; Remote sensing of volcanoes; Volcano monitoring; North America.

1 INTRODUCTION

Medicine Lake Volcano (MLV), northern California, is one of several Cascade volcanoes known to have exhibited ground deformation in recent years. The first levelling measurements at MLV were made in 1954 (Dzurisin *et al.* 1991, 2002) and, with the addition of campaign GPS surveys (Poland *et al.* 2006), comprise a geodetic record that spans 50 yr. Few volcanoes have such long geodetic histories, but what is most unique about MLV is that deformation has been recorded at a constant rate of ~-10 mm yr^{-1} since measurements began.

Past geodetic surveys of the volcano provide an extensive history of ground deformation, with levelling measurements providing good constraints upon the vertical component of deformation, and GPS measurements best constraining horizontal displacements (Poland *et al.* 2006). However, the temporal and spatial resolution of measurements is limited (Fig. 1) and there are discrepancies between the best-fitting analytical models to these past data sets. In this study, we use measurements from interferometric synthetic aperture radar (InSAR), which are made at a much higher spatial density than ground-based surveys. The side-looking nature of InSAR satellites means that measurements contain a component of both horizontal
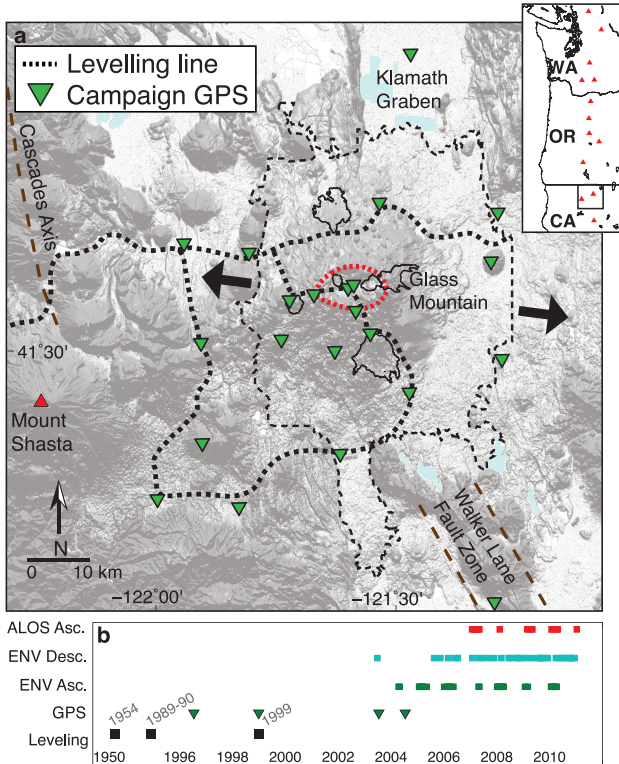
Figure 1. (a) Map of Medicine Lake Volcano (MLV) including main structural features and direction of tectonic extension (after Donnelly-Nolan *et al.* (2008)), plus U.S. Geological Survey geodetic networks. The extent of MLV lavas is shown by dotted black line and the summit caldera is shown by dotted red line. Major holocene lava flows are shown by solid black lines (Donnelly-Nolan 2010) . The site of the last eruption, 1 ka at Glass Mountain, is labelled. These features are overlain on a 30 m SRTM digital elevation model. Inset map shows the location of the main map in relation to the other Cascade volcanoes. (b) Timeline showing the temporal resolution of geodetic data sets at MLV. Levelling measurements are labelled with dates and are from Dzurisin *et al.* (2002). GPS measurements are from Poland *et al.* (2006).

and vertical motion in the line-of-sight (LOS) of the satellite. By combining data acquired from multiple viewing geometries, InSAR measurements have the potential to better constrain both horizontal and vertical deformation fields at MLV (Wright *et al.* 2004b), in addition to providing measurements at a higher temporal and spatial resolution than past ground-based studies.

InSAR is a frequently used volcano monitoring tool, providing measurements of ground deformation in regions both with and without other geodetic equipment (e.g. Sparks *et al.* 2012; Pyle *et al.* 2013; Lu & Dzurisin 2014). For regions that contain numerous volcanoes, such as the Andes or Central America, InSAR may be used to carry out large-scale deformation surveys without the expense or risks associated with deploying equipment on the ground (Biggs *et al.* 2014). However, as is the case in many volcanic settings, the application of InSAR at MLV and throughout the Cascades has been limited by incoherence and noise.

In recent years, various multitemporal analysis methods have been developed to improve the use of InSAR in challenging conditions, and are now becoming widely used due to their accessibility online. This includes those that assume the signal remains constant over time such as: stacking (e.g. de Zeeuz-van Dalfsen *et al.* 2012), rate-map formation (e.g. poly-interferogram rate and time-series estimator: π-RATE; Biggs *et al.* 2007; Elliott *et al.* 2008;

Wang *et al.* 2009, 2012) and persistent scatterer InSAR (Ferretti *et al.* 2001; Hooper *et al.* 2007); and those designed to investigate the temporal evolution of deformation, such as the small baseline subset algorithm (Berardino *et al.* 2002). We test the application of multitemporal analysis methods in the Cascades using multiple sets of InSAR data acquired at MLV, where the apparent steady state of ground deformation and abundance of geodetic data presents an ideal opportunity to assess the application of techniques that assume a linear rate of deformation.

The results of multitemporal InSAR analysis provide improved constraints upon the deformation field at MLV. Comparing the results from InSAR to those of past geodetic studies, we extend the geodetic record to 2011 and determine whether subsidence at MLV continues at historical rates. The improved spatial resolution of InSAR measurements is then used to constrain analytical models of the source of deformation.

1.1 Tectonic and geological setting

Located east of the main Cascades axis on the Modoc Plateau, MLV is considered to be a reararc volcano at the southern end of the Cascade volcanic arc (Donnelly-Nolan *et al.* 2008, Fig. 1a). This region marks the interaction between subduction along the Cascadia subduction zone and extension of the Basin and Range province (e.g. Hildreth 2007), both of which control the structure and behaviour of MLV. The edifice marks a kink in regional fault orientations (Blakely *et al.* 1997) and zones of crustal weakness including a lineament of vents that extend SW to Mount Shasta; the NW extension of the Walker Lane fault zone; and the southern extension of the Klamath Graben (Donnelly-Nolan *et al.* 2008, Fig. 1a).

The total area covered by MLV lavas is >2000 km^2—about 10 times the area of Mount St Helens (Donnelly-Nolan 1988)—and the total erupted volume is estimated to be ∼600 km^3 (Heiken 1978) making MLV the largest volcano by volume in the Cascades (e.g. Donnelly-Nolan 1988; Hildreth 2007). Despite its large volume, MLV is a broad, inconspicuous, volcano with an E-W orientated, 7 × 12 km summit caldera (Fig. 1a).

Volcanism at MLV began about half a million years ago (Donnelly-Nolan & Lanphere. 2005) and the volcano has one of the highest Holocene eruption rates in the Cascades, with nine eruptions having occurred in the last 5.2 ka (Donnelly-Nolan *et al.* 2008). Magmatic products show signatures of both subduction and extension, with hydrous calcalkaline basalts and dry high-alumina olivine tholeitte erupted close together in space and time (Donnelly-Nolan 1988). The most recent eruption at MLV was ∼1 ka at Glass Mountain on the eastern edge of the caldera (Fig. 1a).

1.2 Previous studies of ground deformation at MLV

The U.S. Geological Survey has made repeated measurements of two geodetic networks covering MLV and neighbouring Mount Shasta: a levelling line and a campaign GPS network (Fig. 1b). The first levelling survey of the MLV/Mount Shasta region took place in 1954. Smaller scale surveys were carried out in 1988 in response to a small earthquake swarm, and in 1989–1990, the U.S. Geological Survey Volcano Hazards Program remeasured the MLV circuit (Dzurisin *et al.* 1991, 2002). These surveys revealed volcano wide subsidence and an additional survey of the summit region in 1999 confirmed subsidence at a rate of −8.6 ± 0.9 mm yr^{-1} (Dzurisin *et al.* 2002).

Campaign GPS surveys of the volcano took place in 1996, 1999, 2003 and 2004 (Fig. 1b). The horizontal measurements provided by these GPS campaigns have been essential in discriminating between possible source geometries, as they reveal that deformation at MLV is almost all vertical, with very small horizontal displacements (Poland *et al.* 2006).

Poland *et al.* (2006) present InSAR results in conjunction with their GPS study, summing three temporally consecutive ERS-1/2 interferograms to produce a stack spanning 1993–2000. However, Poland *et al.* (2006) found that ERS-1/2 data exhibit poor coherence in the caldera region, and offer limited additional information to GPS measurements.

## 2 InSAR DATA AND INTERFEROGRAM FORMATION

To address the application of InSAR at MLV, we use the significant archive of InSAR data covering the volcano acquired between 1993 and 2011 by the European Space Agency C-band satellites ERS-1/2 and ENVISAT, plus L-band data from the JAXA satellite ALOS. In total we use: 26 acquisitions from ERS-1/2 descending track 342; 32 acquisitions from ENVISAT ascending track 163; 32 acquisitions from ENVISAT descending track 342 and 15 acquisitions from ALOS ascending track 220 (Fig. 1b). Both C-band satellites have a repeat interval of 35 d but offer variable coverage throughout their operation time. ALOS data span 2007–2011 with a repeat time of 46 d, providing useful constraint on deformation in more recent years.

Interferograms were processed using the JPL/Caltech ROI_PAC software (Rosen *et al.* 2004), filtered using a power spectrum filter (Goldstein & Werner 1998) and unwrapped using a branch cut algorithm (Goldstein & Werner 1988). Topography was removed using a 30 m SRTM DEM (Farr & Kobrick 2000). We guide interferogram formation using time versus perpendicular baseline plots to identify image pairs with short temporal and/or spatial baselines (see Fig. A1 in the Supporting Information). To improve the coherence of C-band interferograms we made alterations to the processing sequence including additional filtering steps, unwrapping manually using bridges to connect isolated coherent patches and increasing the number of looks (coarsening resolution to approx. 300 m, e.g. Goldstein & Werner 1988; Jónsson *et al.* 2002). The final set of C-band interferograms is produced by unwrapping the phase at 16 looks, allowing us to maximize coherence without over smoothing the signal.

2.1 Coherence

The use of InSAR across the Cascades has been limited by incoherence. Coherence is quantified in terms of interferometric correlation, γ, measured across a 3×3 pixel window. For stable pixels, $\gamma = 1$, and for pixels that have independent backscattering phases, $\gamma = 0$ (Seymour & Cumming 1994; Hanssen 2001). We use a threshold of $\gamma = 0.1$, as this produces a smooth phase field in unwrapping while maximizing the number of coherent pixels.

At MLV, incoherence is mostly caused by snow, and dense vegetation, which cause the properties of scatterers to vary over time (temporal decorrelation). Geometrical decorrelation may also result from steep topography, such as the caldera walls. Throughout all data sets we observe good coherence in the arid region surrounding MLV. Pine trees across the flanks and caldera of the volcano significantly reduce the coherence of C-Band data (e.g. Fig. B1 in
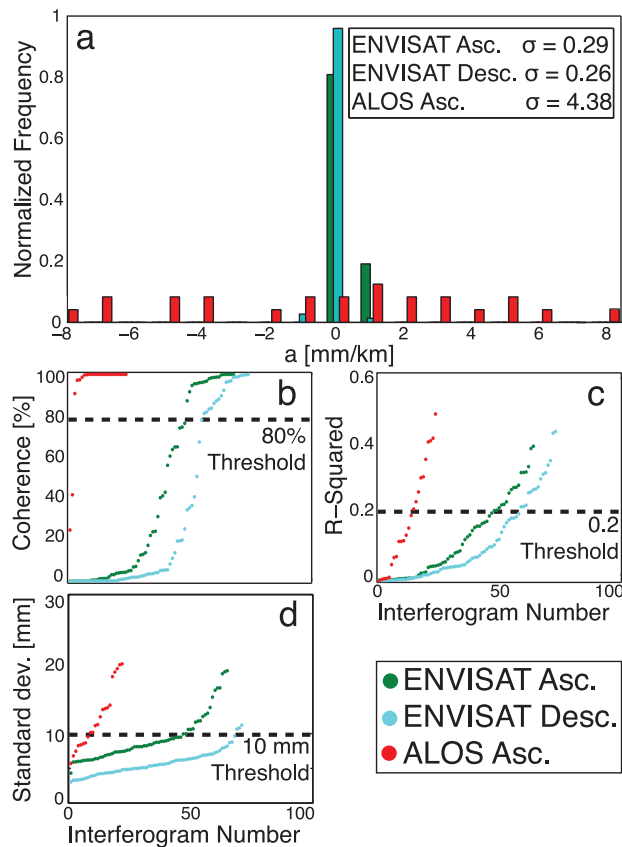
Figure 2. Summary of the coherence and noise of data sets used. (a) Histogram showing the distribution of the orbital parameter a from eq. (2) for each data set. ALOS data have a wider distribution of orbital parameters than ENVISAT as seen by the larger standard deviation. (b–d) Trade-off curves summarizing the coherence and atmospheric noise of each data set. Marked thresholds are those used in noise-based stacking described in Section 3.1.1. (b) Interferograms are ranked by the percentage of coherent pixels in a $0.2° \times 0.1°$ box surrounding the summit caldera. (c) Interferograms are ranked by the r^2 value found by plotting elevation versus phase of each interferogram pixel. (d) Interferograms are ranked by the value of standard deviation found using eq. (3).

Supporting Information), but are less detrimental to L-Band data, as the longer radar wavelength is better able to penetrate vegetation (Massonnet *et al.* 1996; Rosen *et al.* 1996; Ebmeier *et al.* 2013; Lu & Dzurisin 2014). These regions of high elevations are also affected by snow cover between November and May, which impacts all data sets.

We quantitatively assess the coherence of each data set by calculating the percentage of coherent pixels in a $0.2° \times 0.1°$ box surrounding the summit caldera. We then rank the interferograms by coherence and plot a trade-off curve of interferogram number versus coherence (Fig. 2b). L-Band ALOS data exhibits the most complete coherence (more than 90 per cent of interferograms are >30 per cent coherent at the summit), whereas ENVISAT data shows much poorer coherence, with fewer than 45 per cent of ascending track interferograms and 35 per cent of descending track interferograms exceeding 30 per cent coherence at the summit. As was the case for the study of Poland *et al.* (2006), we find that the coherence of ERS-1/2 data at MLV is extremely poor, with fewer than 30 per cent of interferograms exceeding 25 per cent coherence at the summit. In addition to the causes of geometrical and temporal decorrelation highlighted above, such poor coherence can also be

Table 1. Data sets used in this study and associated noise properties described in Section 2. Top: individual interferograms. Bottom: results of π-RATE.

Data set	No. of scenes	Repeat time	Coherence[a]	Orbital parameters[b]			Covar. Function[c]		r^2 [d]
				a	b	c	$\tilde{\sigma}$	$\tilde{\alpha}$	
ENVISAT Asc.	32	35 d	41 per cent	0.29	0.21	2.8×10^4	7.3	16	0.19
ENVISAT Desc.	32	35 d	30 per cent	0.26	0.24	2.3×10^4	5.8	8.3	0.055
ALOS Asc.	15	46 d	90 per cent	4.38	1.88	2.5×10^5	10.8	11.2	0.058
ENVISAT Asc.			100 per cent	0.0025	-0.0007	-0.97	2.96	2.25	2.5×10^{-4}
ENVISAT Desc.			62 per cent	0.0032	-0.0013	-0.81	3.0	6.46	160×10^{-4}
ALOS Asc.			93 per cent	0.0003	0.0011	-1.23	6.8	1.65	4.7×10^{-4}

[a]Percentage of coherent pixels within a $0.2° \times 0.1°$ box surrounding the summit caldera.
[b]Standard deviations of the parameters a, b and c defined in eq. (2) describing the orbital contribution to phase.
[c]Median values of σ and α from eq. (3) describing spatial correlation of the data.
[d]Mean r^2 value describing the correlation between pixel phase and elevation.

attributed to instrument limitations (e.g. Zebker & Villasenor 1992; Hanssen 2001). As the operation time of ERS-1/2 is also covered by levelling and GPS surveys we chose to discard this data set.

2.2 Sources of noise

Interferometric phase is not just a product of ground deformation but also contains several noise terms that compromise accuracy. The LOS displacement (d_{LOS}) may be split into (i) the phase contribution from the difference in ground deformation between acquisitions t_1 and t_2 ($\Delta\phi_{def}$), (ii) the difference in the orbital contribution between acquisitions t_1 and t_2 ($\Delta\phi_{orb}$)(see Section 2.2.1), (iii) the difference in the atmospheric delay between acquisitions t_1 and t_2 ($\Delta\phi_{atm}$) (see Section 2.2.2) and (iv) the phase contribution due to other noise (ϕ_{error}):

$$d_{LOS} = -\frac{4\pi}{\lambda}(\Delta\phi_{def} + \Delta\phi_{orb} + \Delta\phi_{atm} + \phi_{error}). \quad (1)$$

In the following, we analyse the orbital and atmospheric contributions to each data set, with parameters summarized in Table 1.

2.2.1 Orbital errors

Each satellite acquisition is made from a different location above the ground due to forces that act upon the satellite trajectory. Precise orbits are used to determine the exact separation of the satellite orbits, but not all forces can be fully modelled. Our knowledge of the orbital parameters is therefore imperfect, resulting in a long wavelength orbital error that remains in the interferogram (Fig. B1 in the Supporting Information; Zebker *et al.* 1994). As the unmodelled accelerations are small, the error changes slowly in the along track direction (Hanssen 2001) and most authors approximate the orbital contribution using a first- or second-order 2-D polynomial (Biggs *et al.* 2007; Gourmelen *et al.* 2010). Accordingly, we investigate the orbital phase contribution to each data set by finding the perturbation to the orbital parameters which best matches the observed phase using a linear empirical approximation of the form:

$$z = ax + by + c, \quad (2)$$

where $[x,y]$ are the pixel coordinates, a and b are gradient parameters, and c is the intercept. We mask the edifice and solve for a, b and c for each interferogram using a linear least squares inversion. For all data sets we find that both x- and y-gradients have a roughly normal distribution centred on zero (Fig. 2a). Using the standard deviation of the orbital parameters we find that the orbital contributions are greater for ALOS data than for ENVISAT

data (Fig. 2a). This is in agreement with the large perpendicular baselines observed between consecutive ALOS acquisitions when constructing time versus baseline plots, as this indicates a large spatial separation between the satellite orbits (see Fig. A1 in the Supporting Information).

2.2.2 Atmospheric errors

The atmospheric contribution to the phase results from changes in pressure, temperature and water vapour between acquisitions, as each of these factors controls the effective path length between the satellite and the ground. The most variable of these factors is tropospheric water vapour—vertically stratified water vapour causes a phase contribution that tends to correlate with topography, whereas turbulent water vapour causes 3-D heterogeneities in refractivity that manifest as spatially correlated patterns in interferograms (Hanssen 2001). From visual inspection of interferograms at MLV, we find that the main source of atmospheric noise in this setting is turbulent water vapour across the Modoc Plateau, resulting in phase heterogeneities that do not correlate with topography (Fig. B1 in the Supporting Information).

We investigate the effects of water vapour stratification by looking at the relation between elevation and phase in each data set. We begin by removing an orbital phase ramp (as described in Section 2.2.1), masking the edifice and identifying pixels that are coherent in all interferograms. We then use an SRTM 30 m DEM to plot the elevation versus phase of each pixel in the interferogram. We then perform a linear regression to obtain the r^2 value, using this as a measure of the correlation between elevation and phase—interferograms with $r^2 > 0.2$ are deemed to be dominated by atmospheric noise. Using the values of r^2, we rank the interferograms in each data set and plot a trade-off curve of interferogram number versus r^2. As MLV is of relatively low relief compared to the surrounding basin ($\sim$1300 m), we find that most interferograms do not show a strong relation between elevation and phase, and have $r^2 < 0.2$ (Fig. 2c).

In reality, interferograms are highly spatially correlated (Hanssen 2001; Jónsson *et al.* 2002; Lohman & Simons 2005), and to account for spatial correlation of the signal, we use an exponentially decaying form of covariance function to approximate the overall atmospheric phase contribution to each interferogram (Hanssen 2001). We assume that the statistical properties of the atmosphere are radially symmetric (Hanssen 2001) and use a 1-D covariance function of the form:

$$c_{jk} = \sigma^2 e^{(-d_{jk}\alpha)}, \quad (3)$$
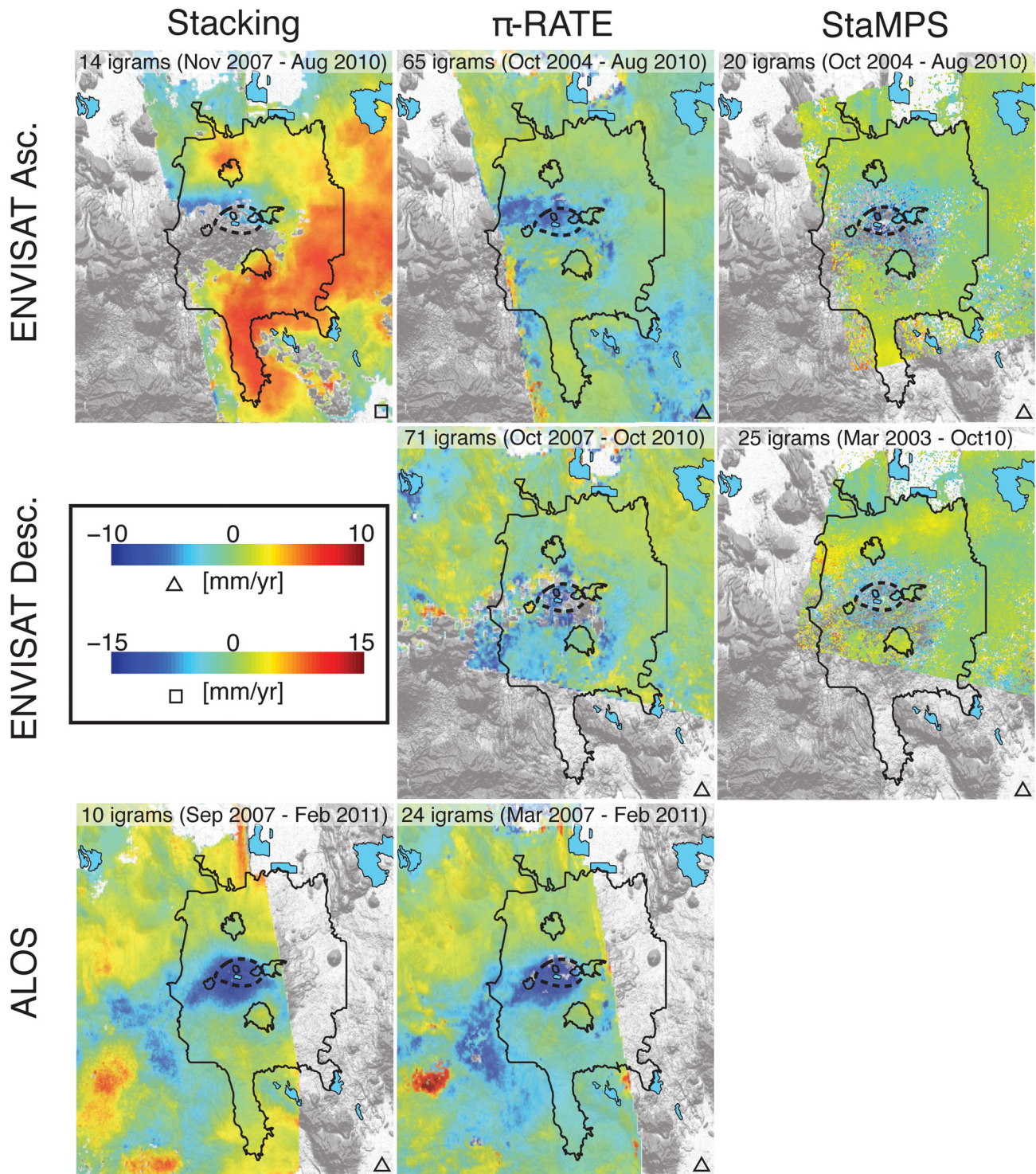
Figure 3. Results of multitemporal InSAR analysis using ENVISAT ascending, ENVISAT descending and ALOS ascending data sets and three methods (noise-based stacking, π-RATE and StaMPS). Each result is labelled with number of interferograms used and dates spanned. Outlined in black are MLV lava flows (solid lines) and caldera (dashed line) as in Fig. 1. Squares and triangles indicate the colour scale used.

where c^{jk} is the covariance between pixels j and k, σ^2 is the variance, d_{jk} is the distance between the pixels and α is the inverse of the e-folding wavelength—a measure of the spatial correlation of the signal. We observe median values of $\sigma = 7.3$ mm and $\alpha = 16.0$ km for ENVISAT ascending data, $\sigma = 5.8$ mm and $\alpha = 8.3$ km for ENVISAT descending data (Fig. 3) and $\sigma = 10.8$ mm and $\alpha = 11.2$ km for ALOS ascending data, all of which are comparable

to the studies of Biggs *et al.* (2007) in Alaska ($\tilde{\sigma} = 7.5$ mm and $\tilde{\alpha} = 12.3$ km) and Lyons & Sandwell (2003) in California ($\tilde{\sigma} = 8.13$ mm).

We use the values of σ^2 to rank the interferograms in each data set by phase standard deviation (σ), plotting a trade-off curve of interferogram number versus standard deviation. We find that all data sets have a similar distribution of standard deviation: the majority

of interferograms have values <10 mm, with standard deviation increasing linearly until the kink in the trade-off curve, at which point we reach interferograms with much higher levels of noise (Fig. 2d).

Both water vapour stratification and turbulence are more significant in regions of significant topography (e.g. Chaussard *et al.* 2013). This is shown by Ebmeier *et al.* (2013), who derive a relation between the relief of the edifice and rms variation in range change across the summit, using examples from volcanoes in Central America. According to this relation, the relief of MLV compared to the surrounding plateau (~1300 m) would result in ~35 mm rms range change variation. This is ~3.5 times larger than the amount of deformation we expect to observe each year at the rates obtained from levelling and GPS, emphasising the importance of using multitemporal methods in this setting.

Numerous studies have developed techniques for reducing the effects of atmospheric noise including: calibration of the signal with an external data source such as GPS (e.g. Li *et al.* 2006); the use of weather models (e.g. Foster *et al.* 2006; Doin *et al.* 2009; Wadge *et al.* 2010) and those based upon the statistical information contained within the interferograms themselves, such as the correlation of phase with topography (e.g. Elliott *et al.* 2008). We take this statistical approach and use three techniques each of which employs statistical information within the interferograms to reduce the effects of atmospheric noise.

3 InSAR METHODS

Various analysis techniques have been developed to improve the coherence and signal-to-noise ratio of InSAR data in problematic settings. Past geodetic studies at MLV suggest that deformation is occurring at a constant rate (Dzurisin *et al.* 2002), and as such we test three techniques that each assume the deformation rate is linear: stacking, rate-map formation (π-RATE; Biggs *et al.* 2007) and the Stanford method for persistent scatterers (StaMPS; Hooper *et al.* 2007). Our choice of these techniques is also motivated by the accessibility of the software, as both π-RATE and StaMPS are available online with an element of user support. Each technique has a different approach to combining interferograms and minimizing the effects of noise; by identifying common features between the results we are able to better determine the extent and magnitude of the deformation field.

3.1 Stacking

A common approach to increasing the signal-to-noise ratio of an InSAR data set is combining multiple interferograms by stacking. This technique has been used elsewhere in the Cascades at Mount St Helens, WA (Poland & Lu 2008), Three Sisters, OR (Riddick & Schmidt 2011) and previously at MLV (Poland *et al.* 2006). This simple method assumes that the signal within the interferograms accumulates at a constant rate while the noise is random. By adding together N interferograms of equal duration, the signal has a magnitude N times bigger than that of an individual interferogram, whereas the noise is only $\sqrt{N}$ times larger (Biggs *et al.* 2007).

Stacking methods can often be further improved by stacking chains of interferograms (e.g. Johanson & Burgmann 2005; Biggs *et al.* 2007), where the slave image of one interferogram is the master image of the next. In this approach, the noise contribution from the slave image of the first interferogram will be cancelled when it is used as the master image of the second interferogram, until the remaining noise contribution is due only to the first and

last acquisitions within the chain. This is beneficial in cases when short duration interferograms are significantly more coherent than longer duration interferograms. This is not the case for the data sets used here, and we find that chain stacking introduces many small unwrapping errors that are of the same magnitude as the subsidence signal across the caldera or, in the case of ALOS, errors due to large perpendicular baselines between consecutive satellite acquisitions.

3.1.1 Noise-based data selection for stacking

Due to the extent of incoherence and phase heterogeneities caused by atmospheric errors, we adopt a stacking strategy designed to optimize the trade-off between the number of interferograms in each stack and the levels of atmospheric noise. This approach is based upon the analysis of coherence and noise sources presented in Section 2.

The main limitation of stacking is that it is only applicable to pixels that are coherent in all interferograms. To combat this we remove any interferograms with <80 per cent coherent pixels in a $0.2° \times 0.1°$ box surrounding the summit caldera. This coherence threshold is selected through a process of trial and error. We begin with a lower value, resulting in poor coherence when we sum all remaining interferograms, and increase this value until we achieve a minimum of ~30 per cent coherence when summing together all remaining interferograms. The result of this step is a smaller but more coherent data set (Fig. 2b).

As the primary cause of atmospheric errors at MLV is atmospheric turbulence, the next step is to use phase variance analysis to remove interferograms that are dominated by large magnitude phase hetrogeneities. When ranking the interferograms by phase standard deviation in Section 2.2.2, we identified a trade-off between the number of interferograms and the maximum standard deviation: including many interferograms increases the maximum standard deviation, whereas including few interferograms reduces the maximum standard deviation but also reduces the temporal coverage of the stack (Fig. 2d). We select a threshold standard deviation to optimize the stack using linear regression to identify the kink in the trade-off curve of each data set. We perform separate linear regressions to the first and last 20 per cent of data points in each data set and use the intersection of these linear regressions to mark a standard deviation threshold. Applying this method to each data set we find that a value of 10 mm provides a good fit to both ALOS and ENVISAT data (Fig. 2d).

The final stage of data selection is designed to minimize the dependence of phase upon topography caused by atmospheric stratification. As discussed previously, most interferograms do not exhibit a strong correlation between elevation and phase ($r^2 > 0.2$; Fig. 2c). We therefore set a threshold of $r^2 = 0.2$, only removing a small set of interferograms with larger r^2 values.

The final stack for each data set is produced by referencing interferograms to a far field region to account for different starting points used in phase unwrapping. We sum the phase at each pixel, divide by the total duration to calculate the rate at each pixel, and finally remove a linear phase ramp to account for the orbital phase contribution. For robustness we use a bootstrap approach to ensure that no single interferogram dominates the final stack. To do this we sequentially remove interferograms from the stack, checking that the maximum LOS displacement remains within 1.5σ of that for the final stack.

In addition to stacking pixels that are coherent in all interferograms, we also test stacks of pixels that are coherent in a certain percentage of interferograms. However, testing different thresholds,

we find that this approach is not robust and results in noisier pixel values that are sensitive to the inclusion or exclusion of single interferograms.

3.2 π-RATE

Whereas the stacking methods described above only retain information from pixels that are coherent in all interferograms, π-RATE employs a pixelwise approach to calculate deformation rates at pixels that are coherent in different numbers of interferograms. This ensures that useful information about the magnitude and spatial extent of the deformation field is not lost. This advanced stacking approach originates from the multi-interferogram method proposed by Biggs *et al.* (2007), with further development by Elliott *et al.* (2008) and Wang *et al.* (2009). The technique has been very successful in measuring fault related processes in regions such as Tibet (e.g. Wang *et al.* 2009; Wang & Wright 2012; Garthwaite *et al.* 2013), but has not previously been applied to volcanic data sets.

Unlike the stacking strategy outlined above, π-RATE corrects for sources of noise using networked corrections rather than removing noisy interferograms. In this approach, constraints from many interferograms are used to calculate the noise contribution at each acquisition rather than at each interferogram (Biggs *et al.* 2007; Wang *et al.* 2009). Networked corrections are used to correct orbital errors and topographically correlated atmospheric errors, which are assumed to vary linearly with height as a first-order approximation (Elliott *et al.* 2008).

π-RATE formally accounts for the error at each pixel using an appropriate variance–covariance matrix, Σ. This contains estimates of spatially correlated noise from the covariance function described in eq. (3), while considering the temporal covariance between interferograms arising from common master or slave dates. The final stack is produced by solving for the best-fitting LOS displacement rate at each pixel, r_{LOS} using a pixelwise linear least squares inversion of the form:

$$\Sigma^{-1}T = \Sigma^{-1}r_{\text{LOS}}P, \tag{4}$$

where T is the duration of each interferogram coherent at that pixel and P is the phase of each interferogram. To improve computation time we downsample the interferograms, testing downsampling factors between 1 and 10. We choose a downsampling factor of 5, optimizing the trade-off between the spatial resolution and computation time. We then solve for all pixels that are coherent in at least two interferograms to maximize the coherence of the signal.

3.3 Persistent scatterer InSAR

The final technique we use is persistent scatterer InSAR (PSInSAR). PSInSAR methods overcome incoherence by identifying persistent scatterer pixels using amplitude and phase stability characteristics (Ferretti *et al.* 2001). Within an interferogram, the phase of each pixel is dependent upon the phase returns from all scatterers in the corresponding element on the ground. Some pixels contain stable scatterers whose phase return remains constant over time despite changes in surrounding scatterers. These persistent scatterers dominate the phase return of the pixel and act to reduce the amplitude and phase variance (Hooper *et al.* 2007).

We use StaMPS developed by Hooper *et al.* (2007), which has proven beneficial in other volcanic settings, such as Three Sisters, OR (Riddick *et al.* 2012), plus several volcanoes in Iceland (e.g. Hooper *et al.* 2009; Ofeigsson *et al.* 2011) and Mexico (Pinel *et al.*

2011), all of which suffer incoherence due to steep topography, snow cover and vegetation. Like π-RATE, this method includes a correction for atmospheric and orbital noise based upon spatial correlation characteristics of the signal (see Hooper *et al.* 2007, for details). We apply StaMPS to all available acquisitions from the ENVISAT ascending, ENVISAT descending and ALOS data sets. Using information from the California Department of Water Resources, we also investigate the effects of snow on PSInSAR by applying StaMPS to a subset of SAR scenes that were acquired during snow-free months. Although this greatly increases the number of PS pixels, the reduced number of SAR scenes compromises estimations of noise terms and we do not take this approach further.
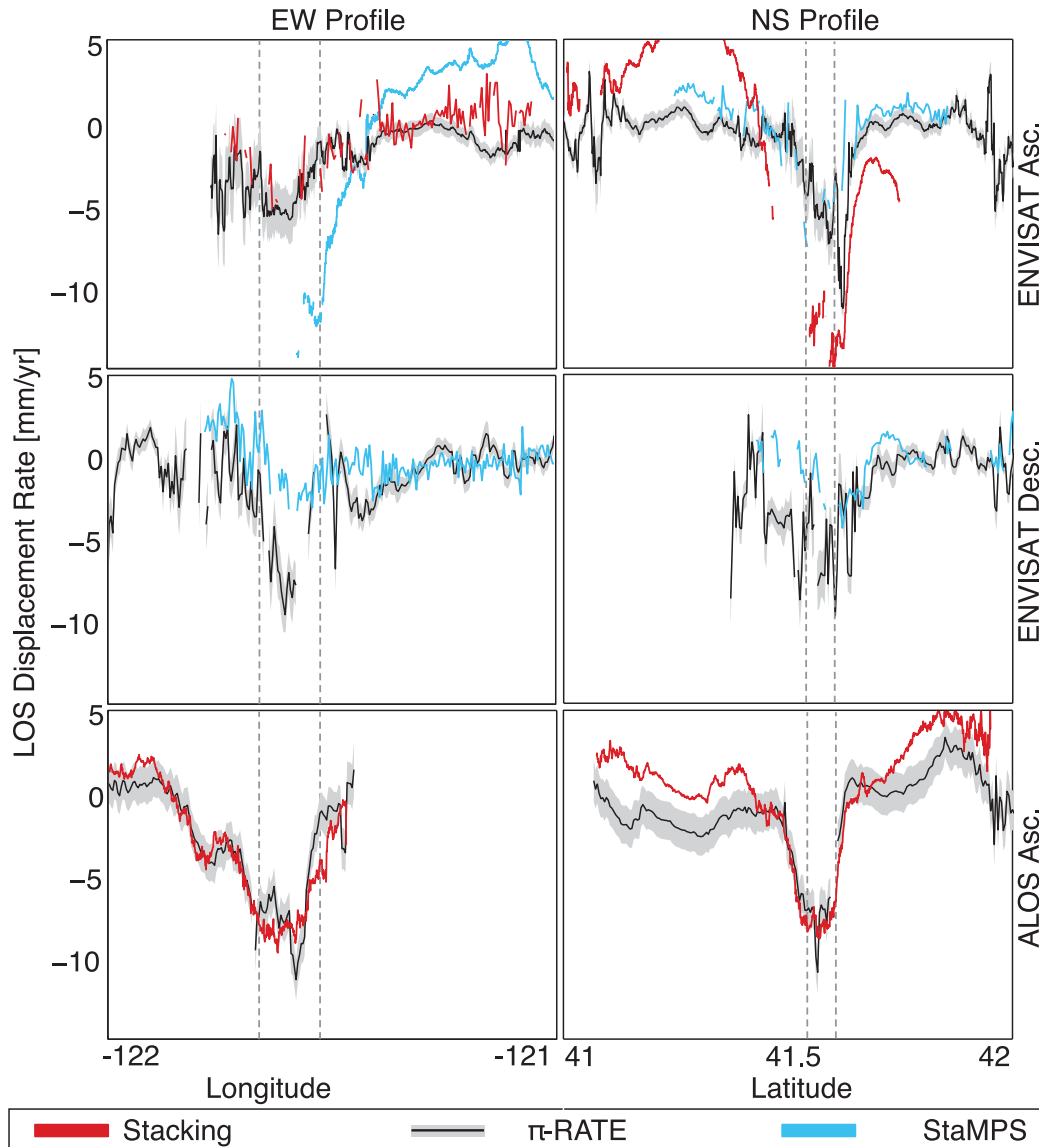
4 RESULTS OF MULTITEMPORAL InSAR ANALYSIS TECHNIQUES

The results from all data sets and analysis methods suggest that ground deformation at MLV continues in the 21st century. All data sets show subsidence of a similar region centred on the summit caldera (Fig. 3), with maximum LOS displacements of ~-13 mm yr^{-1} for ascending data sets and ~-7 mm yr^{-1} for descending data sets. The methods are of variable degrees of success, with π-RATE offering significant improvements to coherence compared to the InSAR results from Poland *et al.* (2006). In this section, we assess the results from each method in terms of the improvement in coherence and the reduction of noise sources. To investigate the magnitude and spatial extent of subsidence recorded by each data set, we take displacement profiles that are coincident with the short and long axes of the caldera (N–S and E–W, respectively; Fig. 4). As was the case for rate-maps, profiles demonstrate broad agreement in the spatial extent of subsidence. The profiles highlight some variability in the magnitude of deformation when using different InSAR analysis techniques, which we attribute to different interferograms being used by each method, but overall the magnitude of deformation is consistent between the three data sets.

4.1 Stacking

Within the stacking results for ENVISAT ascending data, the region SW of the volcano is largely incoherent (Fig. 3). Where there is coherence, displacement profiles show maximum LOS subsidence rates of ~-13 mm yr^{-1}. For ALOS ascending data, which exhibit good coherence at MLV, stacking is more successful, and profiles show maximum deformation rates of ~-9 mm yr^{-1} (Fig. 4). However, subsidence of ~-5 mm yr^{-1} is also observed across the highland between MLV and Mount Shasta (Fig. 3), suggesting that there is a remaining contribution from atmospheric stratification. For profiles of both ENVISAT and ALOS data, we observe other phase signals outside of the caldera, but these are not consistent between data sets and are considered to be due to noise.

Stacks of ENVISAT descending data show significant variability. Using the bootstrap test described in Section 3.1.1, we find that individual interferograms change the LOS deformation rate by $>2\sigma$, as many interferograms exhibit extensive phase heterogeneities, although the overall variance of the data set is similar to that for ascending data (Fig. 2d). The edifice is also surrounded by larger regions of incoherence, and this causes many unwrapping errors in almost all scenes. We therefore find that stacking is not a robust method for dealing with this data set.

Figure 4. Displacement profiles for multitemporal InSAR analysis taken across the long and short axes of the caldera (E–W and N–S directions, respectively). The extent of the caldera is marked on all profiles with dashed grey lines. Error bounds on the results of π-RATE are calculated using the variance–covariance matrix in eq. (4). There is good agreement in the spatial extent of the signal between different InSAR analysis techniques but for ENVISAT data we observe variations in the magnitude of the signal due to different interferograms being used for each method.

4.2 π-RATE

The results of π-RATE for ENVISAT ascending data show almost continuous coherence about the caldera, a significant improvement upon the results of stacking. The magnitude of the deformation signal is reduced by a factor of ~1.5 compared to stacking, which we attribute to a reduction in the effects of atmospheric stratification. However, we do observe anomalous phase signals to the north–west of the caldera which do not correlate with the results of other data sets (Fig. 3). For ALOS ascending data, displacement profiles taken across the results of π-RATE are of comparable magnitude to those for stacking and show similar distributions of displacements (Fig. 4). π-RATE is a much more successful method for ENVISAT descending data than stacking, reducing the effects of atmospheric turbulence and removing unwrapping errors by summing round loops of interferograms and masking any residuals (Biggs *et al.* 2007). Although the results for ENVISAT descending data remain more incoherent and noisy than those for both ascending data sets,

displacement profiles show a clear subsidence signal with maximum LOS displacements of ~-7 mm yr^{-1}, which is in agreement with the results of ascending data (Fig. 4).

4.3 Persistent scatterer InSAR

Applying StaMPS to ENVISAT data significantly improves coherence compared to the raw interferograms, although coherence is not as continuous as for the results of π-RATE. Most PS pixels in the vicinity of the caldera are coincident with large surficial lava flows (Fig. 3), which helps to constrain the extent of the deformation field. Lava flows with fewer PS pixels are sparsely vegetated. From reconnaissance field analysis we find that another possible control upon PS density at lava flows is modal block size—at Burnt Lava Flow, directly south of the caldera, we found that regions with fewer PS corresponded to a smaller modal block size (20–50 cm) compared to the average block size of the flow (50–100 cm). Other

PS pixels are coincident with road intersections, smaller outcrops and clearings within the forest. These findings are similar to those of Riddick *et al.* (2012) in their study of PS in central Oregon, although a possible relation between PS density and block size has not previously been noted.

The deformation field obtained with StaMPS for ENVISAT ascending data has a similar extent to that observed with stacking and π-RATE: deformation is focussed on the caldera, between lava flows to the north, east, south and west, with maximum displacements of ~-8 mm yr^{-1} at Medicine Lake Glass Flow in the NW of the caldera (Fig. 3). However, the anomalous phase signals observed north–west of the caldera in the results of π-RATE have been reduced. Similar results are observed for ENVISAT descending data. Deformation is again constrained within a region bound by lava flows to the north, east, south and west of the caldera, however displacements are of smaller magnitude (up to ~-5 mm yr^{-1}) and there is still some evidence of atmospheric turbulence north of the volcano (Fig. 3). Unlike ENVISAT data, ALOS ascending data are highly coherent at MLV and, due to the success of both stacking and π-RATE, we do not include the results of StaMPS analysis for this data set.

## 4.4 Comparison to past geodetic studies

Past geodetic studies at MLV show that the rate of subsidence remained constant (to within detection limits) between 1954 and 2004 (Dzurisin *et al.* 2002; Poland *et al.* 2006). To assess whether this observation can be extended to 2011, we compare the most coherent set of InSAR results (those produced using π-RATE) to the results of levelling from Dzurisin *et al.* (2002).

The section of the levelling line that covers MLV caldera extends northwards from Burnt Lava Flow south of the caldera, to the centre of the caldera, before continuing west across the long-axis of the caldera (see map in Fig. 5). We select pixels within 1500 m of each levelling station (ensuring that we use the values from >10 pixels) and calculate the average deformation rate before referencing to pixels coincident with the reference levelling station. We assume the deformation is all vertical and, as InSAR measurements are made oblique to vertical, project the levelling measurements into the LOS using the satellite look vector as defined in Wright *et al.* (2004b). Error bars on InSAR measurements are then 1σ calculated by propagating the error values at each pixel, which are obtained using the formal error estimation of π-RATE (eq. 4).

Both ENVISAT data sets are in agreement with the results of past levelling surveys, with maximum displacements coincident with the caldera (Fig. 5). ALOS ascending data are also in close agreement with ENVISAT on the S–N portion of the line. On the E–W portion of the line there is an increase in the magnitude of the signal recorded by ALOS, which we attribute to under correction of residual atmospheric artefacts across the highland between MLV and Mount Shasta (Fig. 5). Overall, we find no evidence of a decrease in the rate of subsidence since 1954, as the results of InSAR analysis fall within error of levelling measurements. This suggests that the constant rate of subsidence detected by Dzurisin *et al.* (2002) continued until at least the last ALOS acquisition in 2011. Deformation at MLV has therefore been sustained at a steady rate for over 60 yr.

4.5 Horizontal and vertical displacements

The side-looking nature of InSAR satellites means that measurements contain a component of both horizontal and vertical motion
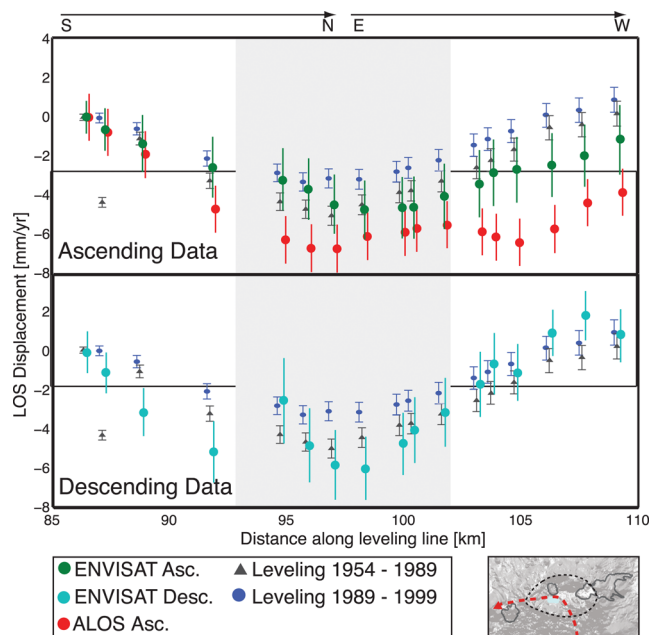

Figure 5. Comparison between the results of levelling from Dzurisin *et al.* (2002) and InSAR. Profiles are offset to aid viewing. The section of the levelling line used is shown by the red line in the small map, where black lines show MLV caldera and lavas as in Fig. 1. The shaded grey region of the profiles corresponds to the extent of the caldera. We average pixels within 1500 m of each levelling station and reference to pixels at the reference levelling station. Errorbars on InSAR measurement are 1σ and are calculated by propagating the error on individual pixels from the variance–covariance matrix in eq. (4).

in the LOS of the satellite (for details see, e.g. Rosen *et al.* 2000). We can therefore use multiple tracks of data, each of which has a different satellite look direction, to decompose the LOS motion into horizontal and vertical components (e.g. Wright *et al.* 2004b; Biggs *et al.* 2009b). This allows us to better constrain the 3-D deformation field at MLV, in addition to providing measurements at a higher temporal and spatial resolution than past geodetic campaigns.

Using the results for ENVISAT ascending and ENVISAT descending data, we solve for the EW and vertical components of motion only, $\mathbf{u} = (u_E, u_Z)^T$, as InSAR measurements are less sensitive to NS motion. We use the equation $\mathbf{R} = \mathbf{Su}$, where $\mathbf{R}$ is a vector of the LOS displacements for each data set and $\mathbf{S}$ is a 2×2 matrix containing the unit satellite look vectors for each data set (Wright *et al.* 2004b). We solve for $\mathbf{u}$ at each pixel, weighting the inversion using a covariance matrix for errors in the observed range change Σ_R (Wright *et al.* 2004b). Σ_R contains values based upon covariance analysis from eq. (3), and is used to find the covariance matrix for the estimated vector components, Σ_u.

The relative magnitudes of the resulting horizontal and vertical displacement fields are in agreement with measurements from levelling and GPS (Fig. 6). GPS surveys of MLV reveal the high ratio of vertical to horizontal displacements (Poland *et al.* 2006) and we find that this is confirmed by InSAR data, with InSAR derived horizontal displacements of ~3 mm yr^{-1}, compared to vertical displacements of up to ~-8 mm yr^{-1} (Fig. 6). Both horizontal and vertical deformation fields are broadly symmetrical and centred on the caldera centre, with vertical deformation extending for ~20 km (Fig. 6).
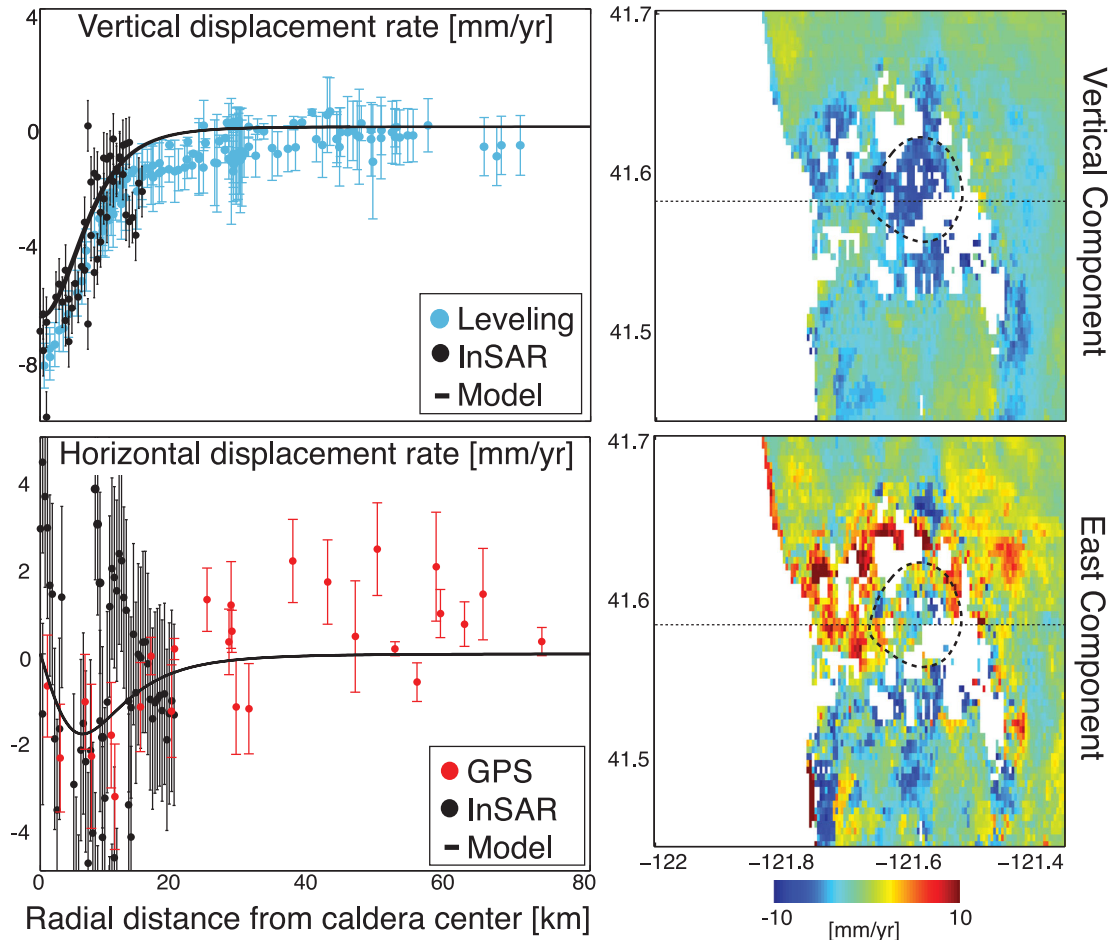
Figure 6. Left: Comparison between the vertical and horizontal components of motion derived from our InSAR study and from past geodetic studies. Levelling measurements are from (Dzurisin *et al.* 2002) and GPS measurements are from (Poland *et al.* 2006). InSAR measurements are from the E–W profiles marked on the rate-maps. Errorbars on InSAR data are found using the covariance matrix Σ_u described in Section 4.5. The solid black line shows model displacements for the best-fitting analytical model to InSAR data described in Section 5.3. Right: maps of vertical and horizontal displacements found by inverting multiple tracks of InSAR data as described in Section 4.5. The caldera is marked by a dashed black line.

5 MODELLING: ESTIMATES OF SOURCE GEOMETRY AND VOLUME CHANGE

The past studies of Dzurisin *et al.* (2002) and Poland *et al.* (2006) consider possible sources of subsidence at MLV. Both authors acknowledge the tectonic contribution due to extension of the Basin and Range province, plus a component of surface loading due to the large volume of emplaced material. However, they also recognize that, to fully explain the deformation field, a component of volume loss at depth is required. The authors model this by first using idealized, elastic models—a well established and widely used approach to obtain information about source geometries from geodetic data (e.g. Dzurisin 2007; Segall 2010). As mentioned previously, there are discrepancies between the best-fitting source models to each data set, as levelling and GPS measurements are sensitive to different components of the deformation field. Both data sets favour a sill rather than a point source, but levelling data prefer a smaller (10.3 × 4.4 km), deeper (11 km) source that strikes NE–SW (221°) (Dzurisin *et al.* 2002), whereas GPS data prefer a larger (18.2 × 9.2 km), shallower (5 km) source that strikes E–W (267°) (Poland *et al.* 2006; Table 2).

We address analytical models of the deformation source using the improved spatial resolution of all available InSAR measurements. As the problem is highly non-linear, we use a Monte Carlo type simulated annealing algorithm as an optimization tool to minimize the misfit function (Amelung & Bell 2003). This combines the efficiency of a derivative-based search algorithm while testing a wide range of source parameters to avoid local minima. We simultaneously solve for all data sets, reducing the number of data points by downsampling (e.g. Biggs *et al.* 2010; Hamling *et al.* 2014, and others). We downsample to a regular grid rather than by quadtree partitioning, as regions of high phase gradients are associated with atmospheric noise in addition to ground deformation. As source models of this nature are inherently non-unique, we investigate the trade-offs between model parameters and the bounds upon each model parameter using a Monte Carlo algorithm (e.g. Wright *et al.* 2004a; Biggs *et al.* 2009a). This is done by using the parametrized values of the covariance function (eq. 3) to create 100 sets of synthetic atmospheric noise for each data set, which are then added to the results selected in Section 5.1 before rerunning the same inversion procedure. The best-fitting parameters and 1σ error bounds from Monte Carlo analysis are summarized in Table 2, and

Table 2. Summary of analytical source models from this study and past geodetic studies. Top: best-fitting point source model. Bottom: best-fitting rectangular sill model. Upper and lower bounds on source parameters to InSAR data are 1σ from Monte Carlo error analysis described in Section 5.

Data	Longitude (°W)	Latitude (°N)	Depth (km)	Length (km)	Width (km)	Strike (°)	Opening (m yr^{-1})	Δ Volume (km^3 yr^{-1})	Misfit[a]
Levelling[1]	121.580	41.590	10	—	—	—	—	−0.0031	18.31
GPS[2]	121.590	41.580	6	—	—	—	—	−0.0010	1.24
InSAR	121.562	41.573	5.8	—	—	—	—	−0.00095	5.33 mm
	121.569	41.576	6.2					−0.0013	
Levelling[1]	121.559	41.566	11	10.3	4.4	221	−0.0446	−0.0020	18.33
	121.410	41.637							
GPS[2]	121.499	41.623	5	18.2	9.2	267	−0.0151	−0.0025	0.96
	121.718	41.616							
InSAR	121.566	41.576	9.1	1.0[b]	1.0[b]	245	−1.10	−0.0011	5.31 mm
	121.572	41.580	9.8			255	−1.33	−0.0013	

[a]Misfit values are not comparable between studies but lower values indicates a better model fit. Misfit for this study is the total rms error between the model and each data set.

[b]Parameter value is fixed in the inversion of InSAR data.

Parameters and bounds are from the following references: [1]Dzurisin *et al.* (2002). [2]Poland *et al.* (2006).

histograms showing the distribution of the model parameters are shown in Fig. C1 in the Supporting Information. Cayol & Cornet (1998) discuss the bias introduced in analytical modelling by steep topography, but we choose not to account for the effects of topography as MLV has low relief compared to the surrounding plateau and topographic slopes do not exceed 2–3°.

5.1 Selection of InSAR data for use in modelling

We use all data sets to model the deformation at MLV, selecting the most successful multitemporal InSAR approach in each case. For ENVISAT ascending data, we use the results of StaMPS, as this offers the best deformation signal, avoiding anomalous phase signals to the north-west of the volcano that are not observed in other data sets (Fig. 3). For ENVISAT descending data, we select the results of π-RATE, as the improvement to coherence is greater than that with StaMPS, as is the reduction of atmospheric turbulence (Fig. 3). Both stacking and π-RATE offer comparable results for ALOS data, but the application of π-RATE has reduced the magnitude of topographically correlated atmospheric delays observed near Mount Shasta (Fig. 3), and we use this as the final input for modelling.

5.2 Point source

We begin by solving for the simplest point source geometry parametrized in terms of: [x,y] location, depth and volume change (Mogi 1958; Dzurisin *et al.* 2002; Poland *et al.* 2006). We allow the location to vary over the extent of the caldera and the depth to vary between 2 and 20 km. The best-fitting source parameters are similar to those found by Dzurisin *et al.* (2002) for levelling data and Poland *et al.* (2006) for GPS data (Table 2), with a source depth of 6 km and rate of volume change of −0.0012 km^3 yr^{-1}. Using Monte Carlo error analysis we find that the location of the source is well constrained SE of the caldera centre (Fig. 7a). We also identify a strong trade-off between depth and source strength as smaller volume changes at shallow depths produce a similar magnitude of deformation as larger volume changes at greater depths (Fig. 7b). Although we do not expect a point source to be the most representative source geometry (Dzurisin *et al.* 2002; Poland *et al.* 2006), the results of this modelling provide good constraints upon the location of the deformation source at MLV.

5.3 Sills

We test more complicated source geometries that are representative of sill-like intrusions, using an approximation of a horizontal, rectangular dislocation (Okada 1985) [the preferred model for both levelling (Dzurisin *et al.* 2002) and GPS data (Poland *et al.* 2006)]. The source is parametrized in terms of: [x,y] location, depth, length, width, strike, dip and opening. We assume a dip of 0° given the apparent symmetry of the deformation signal and the similarity between ascending and descending interferograms. The remaining model parameters are constrained between a set of bounds to reduce the size of the parameter space. We set bounds upon the location using the results of point source modelling described above. For the remaining free parameters (length, width and strike) we run a selected range of forward models, varying a single parameter in each case. We then calculate the rms and plot a curve of rms versus model parameter. Bounds are then set based upon regions of low rms. In addition to geometrical parameters, we specify a Poisson's Ratio of 0.25. As was observed for a point source, solutions are non-unique, and we identify a trade-off between the magnitude of the source and the depth (Fig. 7b).

From Monte Carlo analysis we find that rectangular sills tend towards lengths in excess of 20 km due to residual atmospheric stratification across the highland to the south-west of the volcano, which elongates the subsidence signal (Figs 1a and 4). These lengths are unrealistic: a sill of this size does not fit with models of levelling or GPS data. To overcome this, we rerun the inversion procedure solving for a square sill (length-to-width ratio = 1). We find that square sills with length and width <4 km fit the data to within 1 per cent of the rms for the best-fitting rectangular sill (Fig. 7c).

The best-fitting source geometry found by inverting all data sets is a square sill with length and width 1 km, located at 9.5 km depth with maximum opening of −1.2 m yr^{-1} (Table 2; Fig. 8). This model gives rms values of 1.67, 1.16 and 2.48 mm for ENVISAT ascending, ENVISAT descending and ALOS data sets, respectively (Fig. 8). We estimate the expected error (σ) of each InSAR result using covariance analysis (eq. 3). As each InSAR result is produced using multiple interferograms, the expected error is reduced to $\sigma/\sqrt{N}$, where N is the number of observations and σ is assumed to be uncorrelated between observations (e.g. Parks *et al.* 2011). We obtain expected error values of 1.4, 1.1 and 2.5 mm for ENVISAT ascending, ENVISAT descending and ALOS data sets, which are of
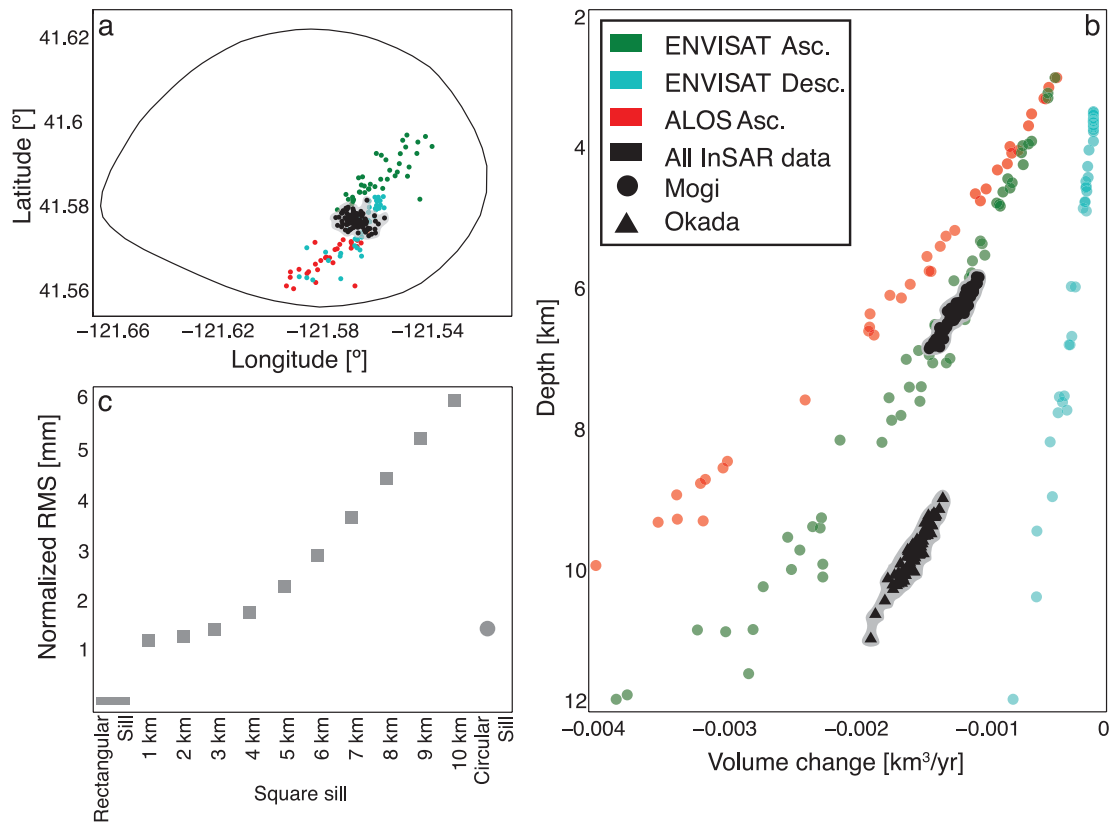
Figure 7. (a) Result of Monte Carlo error analysis for inversions of a point source to constrain the source location. Coloured circles represent inversions of individual data sets and black circles are for joint inversions of all InSAR data. Black line shows the extent of the summit caldera. (b) Trade-off curves obtained from Monte Carlo analysis showing the trade-off between source strength and depth for different source geometries. (c) Summary of the rms misfit for different model geometries found by inverting all InSAR data sets. Square sills with width and length <4 km fit the data to within 1 per cent of the rms misfit for the best-fitting rectangular and circular sills.
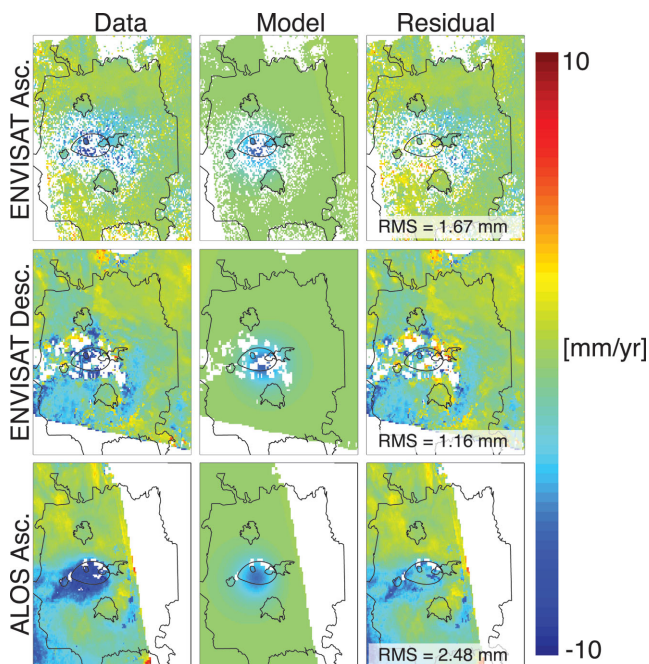
Figure 8. Results of inverse modelling. Data are the InSAR analysis results defined in Section 5.1 and the square sill with parameters specified in Table 2. Plots of residual are labelled with rms values.

the same order as the rms between the best-fitting model and each data set.

The final step of the modelling procedure is to ensure that the model accounts for the high ratio of vertical to horizontal displacements recorded by InSAR. We compare profiles of horizontal and vertical model displacements to the components of motion derived from InSAR data, and also consider the magnitude of horizontal and vertical measurements from GPS and levelling (Fig. 6). The vertical displacements predicted by the model provide a good fit to the vertical measurements from InSAR (rms 1.88 mm), with maximum displacements of ~-7 mm yr^{-1}, and subsidence extending for $\sim$20 km. Model displacements are also mostly within error of the vertical measurements from levelling, although maximum model displacements are 1–2 mm yr^{-1} smaller than those recorded by levelling. The horizontal displacements from InSAR are more variable than the vertical measurements, and are of the same magnitude as the errors (Fig. 6). However, profiles do show that the horizontal model displacements are within the error bounds of the InSAR measurements. In accordance with GPS observations, the horizontal displacements predicted by the model are a factor of $\sim$3 smaller than vertical displacements, and at radial distances <20 km, the model displacements are within error of the GPS measurements.

Through modelling all available InSAR data, we confirm that the best-fitting source geometry at MLV is sill-like. However, uniform opening of a rectangle is not a physically realistic model, and we test this solution against a uniform pressure solution—an axisymmetric, horizontal, penny shaped crack parametrized in terms

of: [*x,y*] location, depth, radius and pressure change (Fialko *et al.* 2001; Biggs *et al.* 2009a). This model has been used in other settings where large ratios of vertical to horizontal displacements have been observed (e.g. Campi Flegrei, Italy; Battaglia *et al.* 2006). We follow the same procedure described above to solve for the best-fitting circular sill and investigate the bounds upon the source parameters. As for the rectangular sill, we find from Monte Carlo error analysis that the sill radius tends towards unrealistically large values, and we therefore opt to constrain the radius of the sill to 1 km, emulating the geometry of the best-fitting square sill. The best-fitting circular sill is located within 1 km of the best-fitting square sill, has the same source depth of 9.5 km and predicts displacements that vary by only up to 1 mm from those predicted by the square shaped sill. This suggests that the depth, location and overall nature of the source are well constrained, but we are unable to distinguish the exact shape of the source.

6 DISCUSSION

Subsidence of MLV is unique in both duration and stable magnitude, with surveys of U.S. Geological Survey geodetic networks since 1954 providing a long and detailed geodetic history of the volcano. The focus of this work has been to use the significant archive of InSAR data acquired at MLV to build upon the long-term record of subsidence, extending the geodetic history to 2011 and investigating the spatial and temporal pattern of deformation at higher resolution. Although the application of these data in this region is problematic, by using a range of data sets from different satellites and a suite of new analysis methods, we have been able to use InSAR data to demonstrate that deformation remains at historical rates of ~ -10 mm yr^{-1}. Of the methods used, we find that π-RATE provides the greatest improvement to coherence, with the coverage of ENVISAT data sets increased by 30 per cent compared to the raw interferograms (Table 1). Comparing the mean values of the orbital and covariance parameters (eqs 2 and 3) before and after application of π-RATE, we also find that this technique reduces the level of noise of each data set (Table 1).

6.1 Causes of subsidence

Past studies attribute subsidence at MLV to a combination of factors including tectonic extension and surface loading, due to the volume of the edifice and its location at the western edge of the Basin and Range extensional province (Dzurisin *et al.* 2002; Poland *et al.* 2006). However, GPS measurements show that there is no resolvable extensional strain across the region (Poland *et al.* 2006), and surface loading is at odds with drill hole data, which suggests that subsidence rates are anomalously high in the present day, as downwarping of the crust beneath the edifice would have occurred within only $\sim$10 per cent of the lifespan of the volcano (Dzurisin *et al.* 2002). Poland *et al.* (2006) suggest that these larger scale processes would enhance subsidence, rather than be the primary cause, and infer an additional component to account for volume loss at depth. Poland *et al.* (2006) and Dzurisin *et al.* (2002) discuss the likelihood of various possible mechanisms: volume loss due to eruption; drainage to a deeper reservoir; hydrothermal fluid withdrawal; and cooling and crystallization at depth. Of these possibilities, Poland *et al.* (2006) deem drainage or cooling and crystallization to be most likely: the last eruption at MLV occurred 1 ka, and the steady nature of the deformation since the 1950s does not agree with a hydrothermal source, as hydrothermal systems gener-

ally exhibit cycles of deformation that occur over shorter timescales (e.g. Dzurisin *et al.* 1999). The hypothesis of cooling and crystallizing magmatic material is also supported by elevated temperatures discovered by geothermal drilling, thought to be due to either the reservoir beneath Glass Mountain or basalt intruded at depth in late holocene times (Donnelly-Nolan *et al.* 1990).

The depth of the modelled source is significant when considering cooling and crystallization as a deformation mechanism at MLV. Rather than the presence of a central magma chamber, the results of geophysical and geological surveys suggest that MLV is underlain by an extensive intrusive complex of sills and dikes with varying compositions (e.g. Finn & Williams 1982; Zucca *et al.* 1986; Fuis *et al.* 1987; Evans & Zucca 1988; Lowenstern *et al.* 2003). Seismic tomography studies of the volcano reveal a small magma body located beneath Glass Mountain (the site of most recent eruption $\sim$1ka) at 3–7 km depth (Evans & Zucca 1988), but they also indicate that a subsolidus pluton could be present within the larger intrusive complex (Ritter & Evans 1997). A shallower source depth may therefore suggest deformation related to material imaged at Glass Mountain, whereas a greater source depth may be indicative of cooling within the underlying intrusive complex.

The best-fitting analytical source model identified in this study fits with the source mechanisms presented by previous authors and accounts for the high ratio of vertical to horizontal displacements derived from InSAR data. The depth of the model (9.5 km) suggests that, if cooling and crystallization is the cause of volume loss, the source is likely to be located within the intrusive complex beneath the volcano, rather than the body of melt imaged at 3–7 km depth. In their study, Dzurisin *et al.* (2002) state that an unrealistically large volume would be required to result in 50 yr of subsidence due to cooling and crystallization. However, simple thermoelastic calculations (e.g. Turcotte & Schubert 2014) do not account for the geotherm, which in this region is thought to be relatively high, or the underlying intrusive complex, which geodetic models suggest is the location of the deformation source. This intrusive complex is described by Poland *et al.* (2006) as a 'relatively hot, roughly cylindrical volume', and is likely to play a role in driving the active geothermal system. Elevated temperatures surrounding the sill would decrease the rate of cooling, as would the production of latent heat during the transition from a liquid to a solid phase. Thus, it is important not to disregard cooling and crystallization as a possible cause of deformation.

7 CONCLUSIONS

This study demonstrates how InSAR data may be successfully applied in mountainous, vegetated regions by using multiple data sets, careful data selection and a suite of multitemporal analysis methods that account for atmospheric and orbital noise sources. Both StaMPS and π-RATE are freely accessible online and offer user support, which plays a fundamental role in helping the community use these methods to better apply InSAR data in challenging regions. The application of these advanced InSAR techniques will be key to the success of data analysis from the new generation of SAR satellites, with the limiting factor likely to be the acquisition rate of the satellite.

Using the results of multitemporal analysis at MLV, we show that the rate of subsidence constrained by InSAR data is comparable to that obtained from levelling studies since 1954 suggesting that current rates of deformation at the volcano have been continuous for over 60 yr. We confirm that, as was observed with

GPS measurements, the deformation field is characterized by high ratios of vertical to horizontal displacements, which is a key constraint upon source models of deformation. We use geophysical inversion methods and Monte Carlo error analysis to obtain the best-fitting source geometry to InSAR data, which we find to be a horizontal sill located at 9.5 km depth beneath the caldera. This geometry accounts for the relative magnitudes of horizontal and vertical components of deformation as recorded by both InSAR and past ground-based surveys. The model is similar to those constrained by past data sets, and fits the hypothesis that deformation at MLV is caused by a combination of tectonic mechanisms, plus a component of volume loss at depth. The most likely cause of volume loss is either drainage or cooling and crystallization of magmatic material. If cooling and crystallization is the cause of present day deformation, the depth of the model suggests that it is related to material within the intrusive complex imaged beneath the volcano.

The next step of studies at MLV will be to use the high resolution of InSAR data and these first-order estimates of source geometry to constrain models of magmatic and tectonic causes of deformation. This will provide further insight into magmatic conditions in northern California, but it is also an opportunity to test hypotheses related to long-term intrusive processes that occur during intereruptive periods (e.g. Caricchi *et al.* 2014).

REFERENCES

Amelung, F. & Bell, J., 2003. Interferometric synthetic aperture radar observations of the 1994 Double Spring Flat, Nevada, earthquake (M5.9): Main shock accompanied by triggered slip on a conjugate fault, *J. geophy. Res.,* **108**(B9), doi:10.1029/2002JB001953.

Battaglia, M., Troise, C., Obrizzo, F., Pingue, F. & De Natale, G., 2006. Evidence for fluid migration as the source of deformation at Campi Flegrei caldera (Italy), *Geophys. Res. Lett.,* **33,** L01307, doi:10.1029/2005GL024904.

Berardino, P., Fornaro, G., Lanari, R. & Sansosti, E., 2002. A new algorithm for surface deformation monitoring based on small baseline differential SAR interferograms, *IEEE Trans. Geosci. Remote Sens.,* **40,** 2375–2383.

Biggs, J., Wright, T., Lu, Z. & Parsons, P., 2007. Multi-interferogram method for measuring inter seismic deformation: Denali Fault, Alaska, *Geophys. J. Int.,* **170,** 1165–1179.

Biggs, J., Anthony, E.Y. & Ebinger, C.J., 2009a. Multiple inflation and deflation events at Kenyan volcanoes, East African Rift, *Geology,* **37**(11), 979–982.

Biggs, J., Robinson, D.P. & Dixon, T.H., 2009b. The 2007 Pisco, Peru, earthquake (M8.0): seismology and geodesy, *Geophys. J Int.,* **176,** 657–669.

Biggs, J., Lu, Z., Fournier, T. & Freymueller, J.T., 2010. Magma flux at Okmok Volcano, Alaska, from a joint inversion of continuous GPS, campaign GPS and interferometric synthetic aperture radar, *J. geophys. Res.,* **115,** B12401, doi:10.1029/2010JB007577.

Biggs, J., Ebmeier, S.K., Aspinall, W.P., Lu, Z., Pritchard, M.E., Sparks, R.S.J. & Mather, T.A., 2014. Global link between deformation and volcanic eruption quantified by satellite imagery, *Nature Commun.,* **5,** doi:10.1038/ncomms4471.

Blakely, R.J., Christiansen, R.L., Guffanti, M., Wells, R.E., Donnelly-Nolan, J.M., Muffler, L.J.P., Clynne, M.A. & Smith, J.G., 1997. Gravity anomalies, Quaternary vents, and Quaternary faults in the southern Cascade Range, Oregon and California; implications for arc and backarc evolutiony, *J. geophys. Res.,* **102,** 22 513–22 527.

Caricchi, L., Biggs, J., Annen, C. & Ebmeier, S., 2014. The influence of cooling, crystallisation and re-melting on the interpretation of geodetic signals in volcanic systems, *Earth planet. Sci. Lett.,* **388,** 166–174.

Cayol, V. & Cornet, F.H., 1998. Effects of topography on the interpretation of the deformation field of prominent volcanoes – application to Etna, *Geophys. Res. Lett.,* **25**(11), 1979–1982.

Chaussard, E., Amelung, F. & Aoki, Y., 2013. Characterization of open and closed volcanic systems in indonesia and mexico using insar time series, *J. geophys. Res.,* **118**(8), 3957–3969.

de Zeeuz-van Dalfsen, E., Pedersen, R., Hooper, A. & Sigmundsson, F., 2012. Subsidence of Askja caldera 2000–2009: modelling of deformation processes at an extensional plate boundary constrained by time series InSAR analysis, *J. Volc. Geotherm. Res.,* **213,** 72–82.

Doin, M.-P., Lasserre, C., Peltzer, G., Cavalie, O. & Doubre, C., 2009. Correction of stratified atmospheric delays in SAR interferometry: validation with global atmospheric models, *J. appl. Geophys.,* **69,** 35–50.

Donnelly-Nolan, J.M., 1988. A magmatic model of Medicine Lake Volcano, California, *J. Volc. Geotherm. Res.,* **93,** 4412–4420.

Donnelly-Nolan, J.M., 2010. Geologic map of Medicine Lake volcano, northern California, *U.S. Geological Survey Scientific Investigations Map 2927,* scale 1:50,000.

Donnelly-Nolan, J.M. & Lanphere, M.A., 2005. Argon dating at and near Medicine Lake volcano, California: results and data, *Open-File Rep,* U.S. Geol. Surv., 1416.

Donnelly-Nolan, J.M., Champion, D.E., Miller, C.D., Grove, T.L. & Trimble, D.A., 1990. Post-11,000-year volcanism at Medicine Lake Volcano, Cascade Range, Northern California, *J. geophys. Res.,* **95**(B12), 19 693–19 704.

Donnelly-Nolan, J.M., Grove, T.L., Lanphere, M.A. & Champion, D.E., 2008. Eruptive history and tectonic setting of Medicine Lake Volcano, a large rear-arc volcano in the southern Cascades, *J. Volc. Geotherm. Res.,* **117**(2), 313–328.

Dzurisin, D., 2007. *Volcano Deformation: Geodetic Monitoring Techniques,* Springer.

Dzurisin, D., Donnelly-Nolan, J.M., Evans, J.R. & Walter, S.R., 1991. Crustal subsidence, seismicity, and structure near medicine lake volcano, California, *J. geophys. Res.,* **96**(B10), 16 319–16 333.

Dzurisin, D., Wicks, J.C. & Thatcher, W., 1999. Renewed uplift at the Yellowstone Caldera measured by levelling surveys and satellite radar interferometry, *Bull. Volc.,* **61**(6), 349–355.

Dzurisin, D., Poland, M.P. & Burgmann, R., 2002. Steady subsidence of Medicine Lake Volcano, Northern California, revealed by repeated levelling surveys, *J. geophys. Res.,* **107**(B12), doi:10.1029/2001JB000893.

Ebmeier, S.K., Biggs, J., Mather, T.A. & Amelung, F., 2013. Applicability of InSAR to tropical volcanoes: insights from Central America, *Geol. Soc., Lond., Special Publications,* **380**(1), 15–37.

Elliott, J.R., Biggs, J., Parsons, P. & Wright, T.J., 2008. InSAR slip rate determination on the Altyn Tagh Fault, northern Tibet, in the presence of topographically correlated atmospheric delays, *Geophys. Res. Lett.,* **35**(12), doi:10.1029/2008GL033659.

Evans, J.R. & Zucca, J.J., 1988. Active high-resolution seismic tomography of compressional wave velocity and attenuation structure at Medicine Lake Volcano, Northern California Cascade Range, *J. geophys. Res.,* **93**(B12), 15 016–15 036.

Farr, T.G. & Kobrick, M., 2000. Shuttle radar topography mission produces a wealth of data, *EOS, Trans. Am. geophys. Un.,* **81**(48), 583–585.

Ferretti, A., Prati, C. & Rocca, F., 2001. Permanent scatterers in SAR interferometry, *IEEE Trans. Geosci. Remote Sens.,* **39**(1), doi:10.1109/36.898661.

Fialko, Y., Khazan, Y. & Simons, M., 2001. Deformation due to a pressurised horizontal circular crack in an elastic half-space, with applications to volcano geodesy, *Geophys. J Int.,* **146**(1), 181–190.

Finn, C. & Williams, D.L., 1982. Gravity evidence for a shallow intrusion under Medicine Lake Volcano, California, *Geology,* **10**(10), 503–507.

Foster, J., Brooks, B., Cherubini, T., Shacat, C., Businger, S. & Werner, C.L., 2006. Mitigating atmospheric noise for InSAR using a high resolution weather model, *Geophys. Res. Lett.,* **33**(16), doi:10.1029/2006GL026781.

Fuis, G.S., Zucca, J.J., Mooney, W.D. & Milkereit, B., 1987. A geological interpretation of seismic refraction results in north-eastern California, *Geol. soc. Am. Bull.,* **98**(1), 53–65.

Garthwaite, M.C., Wang, H. & Wright, T.J., 2013. Broadscale interseismic deformation and fault slip rates in the central Tibetan Plateau observed using InSAR, *J. geophys. Res.,* **118**(9), 5071–5083.

Goldstein, R. & Werner, C., 1998. Radar interferogram filtering for geophysical applications, *Geophys. Res. Lett.,* **25**(21), 4035–4038.

Goldstein, R., Zebker, H. & Werner, C., 1988. Satellite radar interferometry: Two dimensional phase unwrapping, *Radio Sci.,* **23**(4), 713–720.

Gourmelen, N., Amelung, F. & Lanari, R., 2010. Interferometric synthetic aperture radar-GPS integration: interseismic strain accumulation across the Hunter Mountain fault in the eastern California shear zone, *J. geophys. Res.,* **115**(B9), doi:10.1029/2009JB007064.

Hamling, I.J., Wright, T.J., Calais, E., Lewi, E. & Fukahata, Y., 2014. Insar observations of post-rifting deformation around the dabbahu rift segment, Afar, Ethiopia, *Geophys. J. Int.,* **197**, 33–49.

Hanssen, R.F., 2001. *Radar Interferometry: Data Interpretation and Analysis,* Kluwer.

Heiken, G., 1978. Plinian-type eruptions in the Medicine Lake Highland, California, and the nature of the underlying magma, *J. Volc. Geotherm. Res.,* **4**(3), 375–402.

Hildreth, W., 2007. Quaternary magmatism in the Cascades - geological perspectives, *U.S. Geological Survey Professional Paper* 1744.

Hooper, A., Segall, P. & Zebker, H., 2007. Persistent scatterer interferometric synthetic aperture radar for crustal deformation analysis, with application to Volcan Alcedo, Galapagos, *J. geophys. Res.,* **112**(B7), doi:10.1029/2006JB004763.

Hooper, A., Pedersen, R. & Sigmundsson, F., 2009. Constraints on magma intrusion at Eyjafjallajökull and Katla volcanoes in Iceland, from time series SAR interferometry, *The VOLUME Project-Volcanoes: Understanding Subsurface Mass Movement. Dublin: University College,* pp. 13–24.

Johanson, I.A. & Burgmann, R., 2005. Creep and quakes on the northern transition zone of the San Andreas fault from GPS and InSAR data, *Geophys. Res. Lett.,* **32**(14), doi:10.1029/2005GL023150.

Jónsson, S., Zebker, H., Segall, P. & Amelung, F., 2002. Fault slip distribution of the 1999 Mw 7.1 Hector Mine, California, earthquake, estimated from satellite radar and GPS measurements, *Bull. seism. Soc. Am.,* **92**(4), 1377–1389.

Li, Z.W., Ding, X.L., Huang, C., Wadge, G. & Zheng, D.W., 2006. Modeling of atmospheric effects on InSAR measurements by incorporating terrain elevation information, *J. Atmos. Solar-Terrest. Phys.,* **68**(11), 1189–1194.

Lohman, R. & Simons, M., 2005. Some thoughts on the use of InSAR data to constrain models of surface deformation: noise structure and data downsampling, *Geochem., Geophys., Geosyst.,* **6**(1), doi:10.1029/2004GC000841.

Lowenstern, J.B., Donnelly-Nolan, J., Wooden, J.L. & Charlier, B.L.A., 2003. Volcanism, plutonism and hydrothermal alteration at Medicine Lake Volcano, California, in *Proceedings: Twenty-Eighth Workshop on Geothermal Reservoir Engineering,* Stanford Univ., Stanford, CA, p. 8.

Lu, Z. & Dzurisin, D., 2014. *InSAR Imaging of Aleutian Volcanoes: Monitoring a Volcanic Arc from Space,* Springer.

Lyons, S. & Sandwell, D., 2003. Fault creep along the southern San Andreas from InSAR, permanent scatterers and stacking, *J. geophys. Res.,* **108**(B1), doi:10.1029/2002JB001831.

Massonnet, D., Feigl, K.L., Vadon, H. & Rossi, M., 1996. Coseismic deformation field of the M = 6.7 Northridge, California earthquake of January 17, 1994 recorded by two radar satellites using interferometry, *Geophys. Res. Lett.,* **23**(9), 969–972.

Mogi, K., 1958. Relations between eruptions of various volcanoes and the deformations of the ground surfaces around them, *Bull. Earthq. Res. Inst.,* **36**, 99–134.

Ofeigsson, B.G., Hooper, A., Sigmundsson, F., Sturkell, E. & Grapenthin, R., 2011. Deep magma storage at Hekla volcano, Iceland, revealed by InSAR time series analysis, *J. geophys. Res.,* **116**(B5), doi:10.1029/2010JB007576.

Okada, Y., 1985. Surface deformation due to shear and tensile faults in a half-space, *Bull. seism. Soc. Am.,* **75**(4), 1135–1154.

Parks, M.M., Biggs, J., Mather, T.A., Pyle, D.M., Amelung, F., Monsalve, M.L. & Narváez Medina, L., 2011. Co-eruptive subsidence at Galeras identified during an InSAR survey of Colombian volcanoes (2006–2009), *J. Volc. Geotherm. Res.,* **202**(3), 228–240.

Pinel, V., Hooper, A., De la Cruz-Reyna, S., Reyes-Davila, G., Doin, M.-P. & Bascou, P., 2011. The challenging retrieval of the displacement field from InSAR data for andesitic stratovolcanoes: Case study of Popocatepetl and Colima Volcano, Mexico, *J. Volc. Geotherm. Res.,* **200**(1), 49–61.

Poland, M.P. & Lu, Z., 2008. Radar interferometry observations of surface displacements during pre- and coeruptive periods at Mount St. Helens, Washington, 1992–2005, *U.S. Geological Survey Professional Paper,* **1750**, pp. 361–382.

Poland, M.P., Burgmann, R., Dzurisin, D., Lisowski, M., Masterlark, T., Owen, S. & Fink, J., 2006. Constraints on the mechanism of long-term, steady subsidence at Medicine Lake volcano, northern California, from GPS, levelling and InSAR, *J. Volc. Geotherm. Res.,* **150**(1), 55–78.

Pyle, D.M., Mather, T.A. & Biggs, J., 2013. Remote sensing of volcanoes and volcanic processes: integrating observation and modelling-introduction, *Geol. Soc., Lond., Special Publications,* **380**(1), 1–13.

Riddick, S.N. & Schmidt, D.A., 2011. Time-dependent changes in volcanic inflation rate near Three Sisters, Oregon, revealed by InSAR, *Geochem. Geophys. Geosyst.,* **12**(12), doi:10.1029/2011GC003826.

Riddick, S.N., Schmidt, D.A. & Deligne, N.I., 2012. An analysis of terrain properties and the location of surface scatters from persistent scatterer interferometry, *ISPRS J. Photogramm. Remote Sens.,* **73**, 50–57.

Ritter, J.R.R. & Evans, J.R., 1997. Deep structure of Medicine Lake volcano, California, *Tectonophysics,* **275**(1), 221–241.

Rosen, P.A., Hensley, S., Zebker, H.A. & Webb, F.H., 1996. Surface deformation and coherence measurements of Kilauea Volcano, Hawaii, from SIR-C radar interferometry, *J. geophys. Res.,* **101**(E10), 23 109–23 125.

Rosen, P.A., Hensley, S., Joughin, I.R., Li, F.K., Madsen, S.N., Rodriguez, E. & Goldstein, R.M., 2000. Synthetic aperture radar interferometry, *Proc. IEEE,* **88**(3), 333–382.

Rosen, P., Hensley, S., Peltzer, G. & Simons, M., 2004. Updated repeat orbit interferometry package released, *EOS, Trans. Am. geophys. Un.,* **85**(5), doi:10.1029/2004EO050004.

Segall, P., 2010. *Earthquake and Volcano Deformation,* Princeton Univ. Press.

Seymour, M. & Cumming, I., 1994. *Maximum Likelihood Estimation for SAR Interferometry,* pp. 2272–2275, Institute of Electrical and Electronics Engineers.

Sparks, R.S.J., Biggs, J. & Neuberg, J.W., 2012. Monitoring volcanoes, *Science,* **335**(6074), 1310–1311.

Turcotte, D.L. & Schubert, G., 2014. *Geodynamics,* Cambridge Univ. Press.

Wadge, G., Zhu, M., Holley, R.J., James, I.N., Clark, P.A., Wang, C. & Woodage, M.J., 2010. Correction of atmospheric delay effects in radar interferometry using a nested atmospheric model, *J. appl. Geophys.,* **72**(2), 141–149.

Wang, H. & Wright, T.J., 2012. Satellite geodetic imaging reveals internal deformation of western Tibet, *Geophys. Res. Lett.,* **39**(7), doi:10.1029/2012GL051222.

Wang, H., Wright, T.J & Biggs, J., 2009. Interseismic slip rate of the northwestern Xianshuihe fault from InSAR data, *Geophys. Res. Lett.,* **36**(3), doi:10.1029/2008GL036560.

Wang, H., Wright, T.J., Yu, Y., Lin, H., Jiang, L., Li, C. & Qiu, G., 2012. InSAR reveals coastal subsidence in the Pearl River Delta, China, *Geophys. J. Int.,* **191**(3), 1119–1128.

Wright, T., Lu, Z. & Wicks, C., 2004a. Constraining the slip distribution and fault geometry of the Mw 7.9, 3 November 2002, Denali Fault earthquake with interferometric synthetic aperture radar and global positioning system Data, *Bull. seism. Soc. Am.,* **94**(6B), S175–S189.

Wright, T.J., Parsons, B.E. & Lu, Z., 2004b. Toward mapping surface deformation in three dimensions using InSAR, *Geophys. Res. Lett.,* **31**(1), doi:10.1029/2003GL018827.

Zebker, H.A. & Villasenor, J., 1992. Decorrelation in Interferometric Radar Echoes, *IEEE Trans. Geosci. Remote Sens.,* **30**(5), 950–959.

Zebker, H., Rosen, P. & Goldstein, R.M., 1994. On the derivation of co-seismic displacement fields using differential radar interferometry: The Landers earthquake, *J. geophys. Res.,* **99**(B10), 19 617–19 634.

Zucca, J.J., Fuis, G.S., Milkereit, B., Mooney, W.D. & Catchings, R.D., 1986. Crustal structure of northeastern California, *J. geophys. Res.,* **91**(B7), 7359–7382.

SUPPORTING INFORMATION

Additional Supporting Information may be found in the online version of this article:

APPENDIX A: Time versus perpendicular baseline plots.
APPENDIX B: Example of noise observed in interferograms.
APPENDIX C: Histograms of source parameters for analytical modelling (http://mnras.oxfordjournals.org/lookup/suppl/doi:10.1093/mnras/ggu304/-/DC1).

Please note: Oxford University Press is not responsible for the content or functionality of any supporting materials supplied by the authors. Any queries (other than missing material) should be directed to the corresponding author for the article.